Thrust deduction analysis for wind-assisted ships

(article starts on next page)

Thrust deduction analysis for wind-assisted ships

Abdoul-Malik Bakari[1], **Rui Lopes**[1], **Alex Abolfazl Shiri**[2], **Arash Eslamdoost**[1]

[1]Division of Marine Technology, Department of Mechanical Engineering, Chalmers University of Technology, Gothenburg, Sweden
[2]RISE Research Institutes of Sweden, Gothenburg, Sweden

ABSTRACT

Wind-assisted ship propulsion (WASP) presents a promising option for reducing emissions and decarbonizing the maritime industry. To better understand how wind sails influence ship performance, this study examines the effect of leeway angle on thrust deduction. The side forces and resistance components are also analyzed.

Computational Fluid Dynamics (CFD) simulations based on the Reynolds-Averaged Navier–Stokes (RANS) equations are conducted at model scale for the JoRes1 tanker at Froude number of 0.162. To minimize computational costs, a double-body approach is used, ignoring free-surface effects, and the propeller is modeled with a virtual disk approach. Resistance and self-propulsion simulations are performed across a range of leeway angles and sail thrust levels. The results indicate that the leeway angle affects resistance and side forces, with pressure resistance becoming more dominant at larger leeway angles. The traditional thrust deduction formula is shown to be inadequate for wind-assisted propulsion, as it produces values that differ from those of conventional vessels under high sail thrust. A modified thrust deduction formulation provides a more consistent representation of propulsion performance. The modified thrust deduction factor t^* and the resistance increment coefficient r are more appropriate for analyzing the effects of the leeway angle and sail thrust on ship resistance and propeller thrust.

Keywords

Ship hydrodynamics, Leeway angle, Resistance, Thrust deduction, Wind-assisted ships.

1 INTRODUCTION

Global shipping produces about 3% of the world's Greenhouse Gas (GHG) pollution (Fadaie et al. (2025)), and the industry aims to reach net-zero emissions by 2050. One alternative proposed by the International Maritime Organisation (IMO) is to use wind as an energy source for commercial ships (IMO, 2023). WASP can reduce fuel consumption by 8.5% to 16.2%, as well as NOx and CO_2 emissions by 17% per year (Ammar and Seddiek, 2022). Under appropriate wind conditions, it may even reduce fuel consumption by 30% (Ouchi et al., 2013). To fully take advantage of WASP, it is crucial to develop a comprehensive understanding of how wind sails impact both hydrodynamic and aerodynamic effects.

A ship's performance must be analyzed under various loading conditions to properly integrate a wind-assisted propulsion system. Running numerical simulations for these different conditions is therefore a necessary and important step. While the aerodynamic aspect of WASP has been widely addressed in recent work for example, Bordogna (2020) studied sail aerodynamics, very few studies have addressed the hydrodynamic effect. According to Clayton (1987), when a ship operates with sails, the hull is subjected to aerodynamic side forces, resulting in leeway and a heel angle relative to the direction of motion. The effect of leeway and heel angle on a bare hull has been investigated by Saydam et al. (2022). Their results show that the heel angle has less effect on resistance and side force when heel is below 10 degrees; however, variations in leeway angle cause significant changes in forces. Additionally, bare hull simulations conducted by Bakari et al. (2025) studied the effect of leeway angle on forces, finding that at high leeway angles the side force can be two times higher than the resistance force. Overall, many investigations have been made for bare hull simulations, but very few numerical studies have addressed self-propulsion.

Most of today's ship design and analysis tools assume unchanged propulsive factors for WASP for different wind contributions. The objective of this study is to evaluate the accuracy of this assumption by investigating the leeway angle effect on ship thrust deduction and forces. This includes how to define the thrust deduction for WASP and how thrust deduction changes with leeway and different sail thrust conditions. It also involves analyzing the side force and resistance components.

2 METHODOLOGY

This section presents the numerical approach used to study the propeller–hull interaction under drift and wind-assisted conditions. It describes the ship geometry, computational domain, mesh, and virtual propeller model. It also explains the definition of sail thrust, the assessment of numerical uncertainty, and the evaluation of thrust deduction and changes in resistance.

2.1 Test case

The ship geometry used in this study is the single-screw JoRes1 tanker shown in Figure 1, with simulations conducted at model-scale with a scale factor of 26 (JoRes (2023)). The ship's speed corresponds to a Froude number of 0.162. The details of the ship are presented in Table 1. This geometry is an mono asymmetric hull. The propeller is a 4 blades propeller and at full scale has a diameter of 6.5m. The propeller rotates in the clockwise direction. The main particulars of this propeller are shown in Table 2.

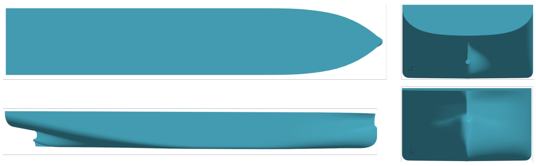

Figure 1: Jores1 Tanker geometry

Table 1: Full-scale and model-scale particulars of JoRes1 tanker

Parameter	Full scale	Model scale
Length between perpendiculars Lpp (m)	178.50	6.86
Breadth B(m)	32.26	1.24
Draught at fore perpendicular T_{FP} (m)	10.56	0.406
Draught at aft perpendicular T_{AP} (m)	10.38	0.399
Draught at midship T_M(m)	10.47	0.402
Wetted surface area S (m^2)	8337.10	12.68
Displaced volume ∇ (m^3)	46648	2.86
Speed V (m/s)	6.82	1.346

Table 2: Main particulars of propeller

Parameter	Full Scale	Model Scale
Diameter, D_P (m)	6.50	0.250
Mean pitch ratio, P_P/D_P	0.790	0.790
Hub diameter ratio, D_H/D_P	0.140	0.140
Disc area ratio, A_E/A_0	0.449	0.449
Number of blades, N_{PB}	4	4

2.2 Numerical setup

The numerical simulations were performed using Simcenter STAR-CCM+ (version 2024.10.1). In this study, the flow of an incompressible Newtonian fluid is considered. Because of the high Reynolds number and the dominant influence of turbulence, the Reynolds-averaged Navier–Stokes (RANS) equations are solved. To reduce the computational cost, the free surface is not included in the simulations; therefore, a double-body approach is adopted and free-surface effects are neglected. This approach is widely used for the computation of self-propulsion problems according to Yao et al. (2016), and provides reasonable results. The governing equations are discretized using the finite volume method. A segregated solver based on the SIMPLE algorithm is employed for pressure velocity coupling. All simulations are performed under unsteady conditions with a time step of 0.01 s. The y^+ target is maintained below 1, ensuring a wall-resolved approach for all simulations. The k-ω SST turbulence model is employed throughout the study, as recommended by the ITTC (2011) guidelines. The water density ρ is set at 999 kg/m^3.

The computational domain is defined following the recommendations of ITTC (2022) as shown in Figure 2. The total domain length is equal to 6 L_{pp}, with 2 L_{pp} from the inlet to the hull and 3 L_{pp} from the ship to the outlet. The distance from the side boundaries and the bottom to the ship is set to 2 L_{pp}. The top boundary is located at the draft position. The applied boundary conditions, the propeller position, and the flow direction are also illustrated in Figure 2. The coordinate system used to evaluate the forces and define the leeway (drift) angle is presented in Figure 2b. The drift angles covered in the computations are 0°, 2°, 4°, 6°, 8°, 9°, −2°, −4°, −6°, −8° and −9°. The computational mesh, shown in Figure 3, consists of unstructured trimmed hexahedral cells with local refinements around the propeller and near the hull. Prism layers are generated along the hull surface to properly resolve the boundary layer. All meshes are created using the automatic mesh generator in STAR-CCM+.

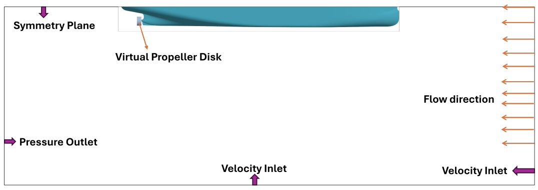

(a) Boundary conditions (Side view)

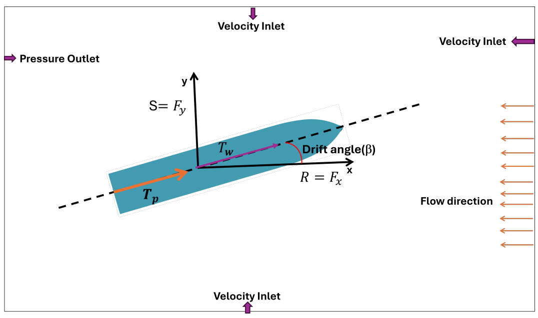

(b) Boundary conditions and coordinate system (Top view)

Figure 2: Computational domain, boundary conditions and coordinate system

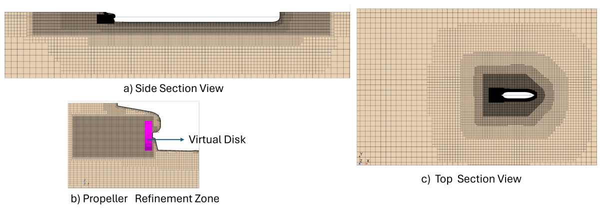

Figure 3: The mesh details

2.2.1 Virtual propeller setup

The open water curve data used to setup the virtual disk setup are from the experimental model test conducted by Hamburgische Schiffbau-Versuchsanstalt GmbH HSVA (2023). The propeller open water tests are conducted to quantify how the propeller performs in isolation, free from hull-induced wake effects. The Figure 4 shows the measured thrust K_T, torque K_Q, and efficiency η_0 of the open water test.

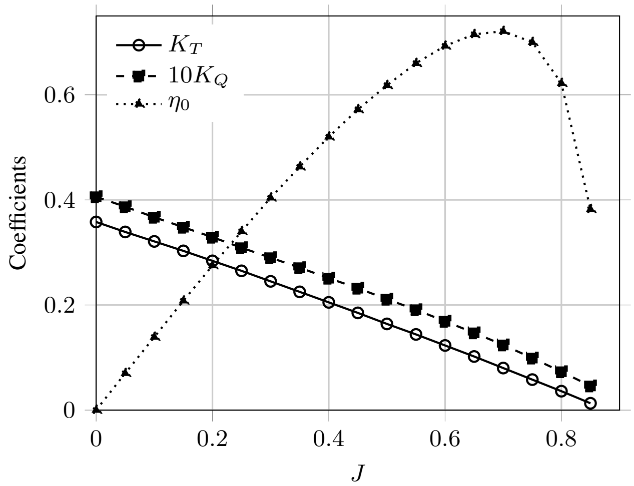

Figure 4: Open water curve of the JoRes 1 tanker propeller

2.3 sail thrust definition

To evaluate the impact of sail thrust on propeller–hull interaction, no actual sail model is used in this work. Instead the propeller is unloaded at a constant ship speed by applying an external force representing the sail thrust. A PID controller is used to control the propeller rotation rate to provide the thrust needed to balance the forces in the x direction, as shown in Figure 2b. The resistance obtained at self-propulsion for a drift angle of 0°, R_{SF_0}, is used as a reference to estimate the sail thrust. The target sail thrust is defined as:

$$T_w = p_w(R_{SF_0} - R_A), \tag{1}$$

where R_A is the towing force and p_w the percentage of sail thrust. R_{SF_0} is a constant reference value.

2.4 Thrust deduction definition

The thrust deduction (t) represents the ratio between the resistance of the ship (R_{BH}) and the thrust produced by a ship's propeller (T_p). As also shown in 1, by convention, the hydrodynamic resistance of a ship is defined in the direction of advance, while the propeller thrust is defined along the propeller shaft axis. It expresses the ratio between bare-hull resistance and propeller thrust. A large thrust deduction implies strong propeller-hull interaction effects, and vice versa.

According to the ITTC (2022), the conventional thrust deduction is defined as:

$$t = 1 - \frac{R_{BH} - R_A}{T_p}, \tag{2}$$

When wind sails provide additional thrust to the ship, the sail thrust T_w must be included in the thrust deduction formulation. Sauder and Alterskjær (2022) accounted for this effect by redefining the thrust deduction fraction as:

$$t^* = 1 - \frac{R_{BH} - R_A - T_w}{T_p}. \tag{3}$$

In addition to this formulation, a new expression is proposed in the current work to quantify the resistance change between bare hull and self-propelled hull associated with changes in hull equilibrium position and sail thrust. This quantity, referred to as the resistance increment coefficient r, is defined as:

$$r = 1 - \frac{R_{BH}}{R_{SP}}, \tag{4}$$

where, R_{SP} is the resistance in self-propulsion. R_{SP} can be obtained from a numerical simulation; however, it is not straightforward to measure in a towing tank test.

2.5 Numerical uncertainty

The numerical uncertainty in the CFD simulations must be carefully evaluated. Numerical uncertainty defines an interval that is expected to contain the true or exact solution. In this study, the numerical uncertainty is calculated to assess simulation accuracy using the procedure developed by Eça and Hoekstra (2014). Due to the unstructured grid topology, exact geometric similarity could not be achieved, although all other parameters were kept as consistent as possible. Following the procedure of Eça and Hoekstra (2014), four systematically refined grids were generated to enable numerical uncertainty estimation for thrust and hull forces. The refinement process started from a coarse baseline grid of approximately 2 million cells (Table 3), with each subsequent grid created by applying a constant refinement ratio of $\lambda = \sqrt{2}$ to the characteristic cell size. Following this systematic approach, the finest grid in the sequence reached approximately 33.3 million cells after three refinements.

3 RESULTS AND DISCUSSION

This section presents the numerical results of the bare hull and self-propelled simulations. First, a verification study is conducted to assess the numerical uncertainty of the CFD simulations. Following this, the force components (resistance and side force) are analyzed for both bare-hull and self-propelled configurations at various drift angles and sail thrust conditions. Finally, the thrust deduction is examined, comparing classical and modified formulations to highlight the implications for wind-assisted ship performance assessment.

3.1 Uncertainity analysis

Verification is carried out to assess the numerical accuracy of the simulations. For different drift angles, the number of cells may vary slightly and the flow behaviour may differ. For this reason, the numerical uncertainty analysis is conducted for drift 0° and drift 9° under zero sail thrust conditions.

Tables 3 and 4 present the uncertainty analysis for drift angles 0° and 9°, respectively. The analysis includes resistance components, namely pressure resistance (R_P), frictional resistance (R_F), and total resistance (R), as well as side force components: pressure side force (S_P), frictional side force (S_F), and total side force (S). Additional parameters such as propeller thrust and propeller rotational speed (n) are also considered. The total resistance (R) is equal to the longitudinal force F_x, and the total side force (S) is equal to the transverse force F_y, as shown in Figure 2b.

The grid uncertainty study is performed using four grid refinements with total number of cells equal to 2.2, 5.08, 12.7, and 33.3 million cells. The numerical uncertainty is evaluated on the third, less fine grid (U_3), which contains approximately 5 million cells. For most parameters, the numerical uncertainty remains below 20%, except for the side force components. At drift 0°, the side force is very close to zero and would ideally be zero for a perfectly symmetric geometry. However, the JoRes1 Tanker is an asymmetric ship, which leads to a non-zero estimation of the side force at zero drift. Due to the very small value of the side force at drift 0°, the associated uncertainty is high and not listed in Table 3, mainly because pressure forces can change sign and are difficult to estimate accurately at such low values. At drift 9°, the uncertainty of the side force is reduced to approximately 17%. At this drift angle, the side force magnitude is sufficiently large, making its estimation more reliable and less sensitive to numerical fluctuations.

Table 3: Discretization error for different quantities at drift angle 0°

Parameter	Grid Resolution [million cells]				U_3 [%]
	2.21	5.08	12.7	33.3	
R_P (N)	8.752	8.913	9.083	9.207	8.2
R_F (N)	28.786	30.779	32.160	33.054	19.6
R (N)	37.538	39.693	41.243	42.260	18.3
T_p (N)	24.518	26.669	28.216	29.236	13.6
S_P (N)	1.341	2.464	2.330	2.422	-
S_F (N)	-0.001	-0.001	-0.001	-0.001	-
S (N)	1.341	2.462	2.329	2.422	-
n (rps)	7.125	7.295	7.351	7.395	5.7

Table 4: Discretization error for different quantities at drift angle 9°

Parameter	Grid Resolution [million cells]				U_3 [%]
	2.21	5.08	12.7	33.3	
R_P (N)	22.653	23.032	23.032	23.054	6.5
R_F (N)	29.933	32.022	33.366	34.276	16.5
R (N)	52.586	55.054	56.398	57.330	12.9
T_p (N)	39.567	42.034	43.378	44.319	17.3
S_P (N)	87.022	88.449	88.220	87.945	4.8
S_F (N)	-1.776	-1.723	-1.676	-1.643	16.7
S (N)	85.246	86.726	86.544	86.302	5.1
n (rps)	8.091	8.224	8.274	8.321	4.2

Figure 5 shows the total resistance. This quantity is presented as examples to illustrate how the uncertainty ranges are delimited for drift angles of 0° and 9°. The fine grid is taken as the reference case with a relative grid size of 1, while the coarse grid has a step size of approximately 2.5. The uncertainty range is calculated based on the third refinement level, corresponding to the mesh with approximately 5 million cells. All following simulations are therefore performed using the 5 million cells grid.

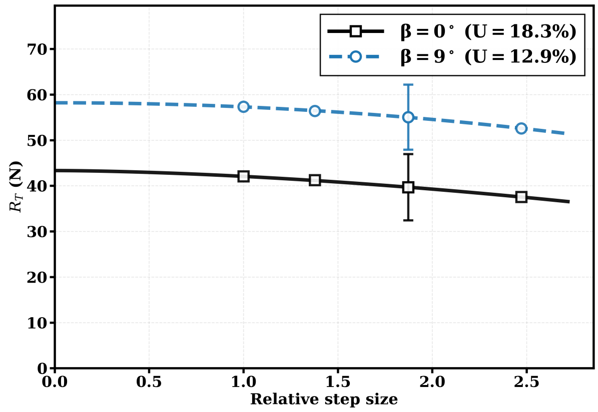

Figure 5: Convergence with the grid refinement of total self-propulsion resistance at drift angle 0° and 9°

3.2 Forces Components Analysis

Bare hull simulations are conducted to estimate the effects of the leeway angle on resistance and side force. The resistance coefficient is computed using Equation 5 and is obtained as the sum of the friction (C_{r_f}) and pressure (C_{r_p}) components. The side force coefficient is computed using Eq. 6 and is decomposed into friction (C_{s_f}) and pressure (C_{s_p}) components.

$$C_r = \frac{R}{\frac{1}{2}\,\rho\,S_w\,V^2}, \tag{5}$$

$$C_s = \frac{S}{\frac{1}{2}\,\rho\,S_w\,V^2}, \tag{6}$$

where S_w is the wetted surface area of the model.

Figure 6 shows the bare-hull resistance components. The total resistance increases significantly with increasing drift angle, reaching 36% increase at a drift angle of 9° compared to 0°. The component that changes the most is the pressure resistance (C_{r_p}), which increases by up to 200% from drift angles 0° to 9°. In contrast, the frictional resistance (C_{r_f}) remains almost unchanged, with a variation of only about 3%.

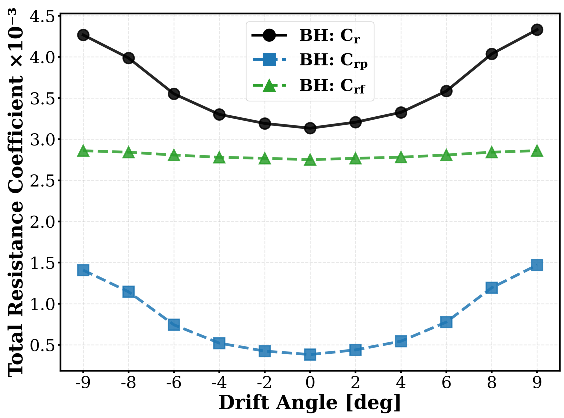

Figure 6: Bare hull (BH) resistance component coefficients with drift angle variation

Self-propulsion simulations are conducted for different propeller unloading conditions. The Virtual Disk propeller model in STAR-CCM+ combined with a PID controller is used to automatically control the propeller thrust to balance the forces in x-direction. Each sail thrust condition corresponds to a sail thrust contribution T_w.

Figures 7a, 7b, 7c, and 7d show the bare hull and self-propelled hull resistance components for sail thrust contributions of 0%, 10%, 30%, and 50%, respectively. Due to propeller induced suction in the aft, the total resistance coefficient in self-propulsion is larger for all the self-propulsion conditions compared to the bare hull. The pressure component is the least dominant contribution to the total resistance but increases significantly, with an average increment of approximately 40% as the drift angle increases. As shown in Figure 8, the frictional resistance component increases almost linearly with increasing drift angle. This corresponds to about 4% increase from drift angle 0° to 9°. The frictional resistance coefficient of self-propelled hull remains nearly unchanged with varying sail thrust relative to the bare hull frictional resistance coefficient at the same drift angle.

Figure 9 presents the pressure resistance for all cases. The self-propulsion pressure resistance is highest at large drift angles in the absence of sail thrust. The self-propulsion pressure resistance is significantly increased, reaching up to 80% compared to the bare-hull case at a drift angle of 0°. As the sail thrust increases, the resistance begins to decrease.

The hull side force is strongly influenced by increasing leeway angle. Figure 10 shows the side force coefficient C_s for bare-hull as well as self-propelled hull at different leeway angles. The side force increases almost linearly with increasing drift angle and grows at more than twice the rate of the resistance force coefficient C_r. Interestingly, in self-propulsion, the side force increases by approximately 5% compared to the bare-hull at $\pm 9°$ drift. The side force is slightly larger at positive drift angles in comparison to negative drift angles, which is attributed to the asymmetric geometry of the hull. The increase in side force under self-propulsion conditions may be attributed to the contribution of the propeller-induced side force.

Figure 11 shows the pressure distribution over the aft part of the hull, at 0% and 50% sail thrust for drift angle 0°. A small pressure difference is observed between these propeller loading conditions, with higher pressure levels occurring at 50% sail thrust. This occurs due to the reduced propeller suction effect for the unloaded case.

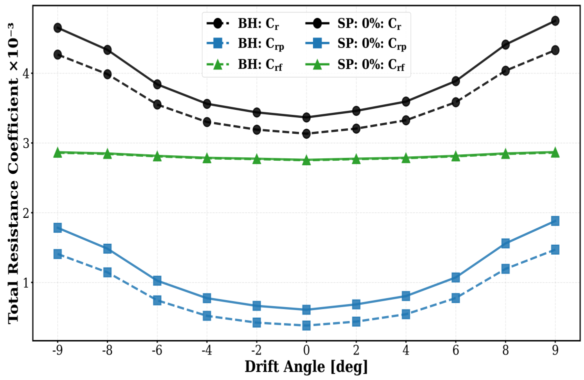

(a) 0% Sail thrust

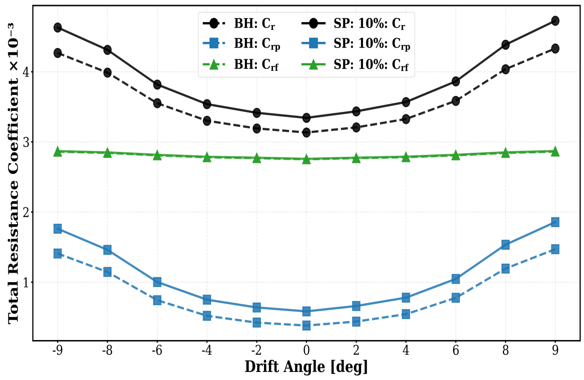

(b) 10% Sail thrust

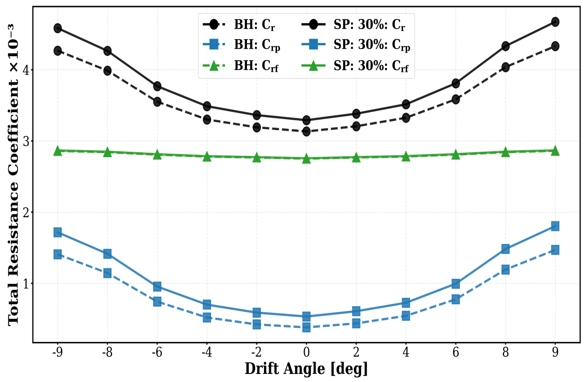

(c) 30% Sail thrust

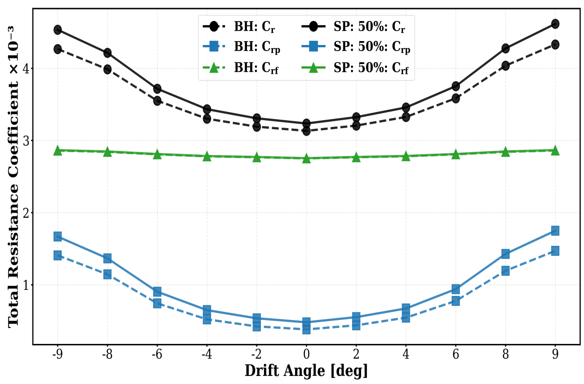

(d) 50% Sail thrust

Figure 7: Bare hull (BH) and self-propelled hull (SP) resistance components against drift angle for different sail thrust

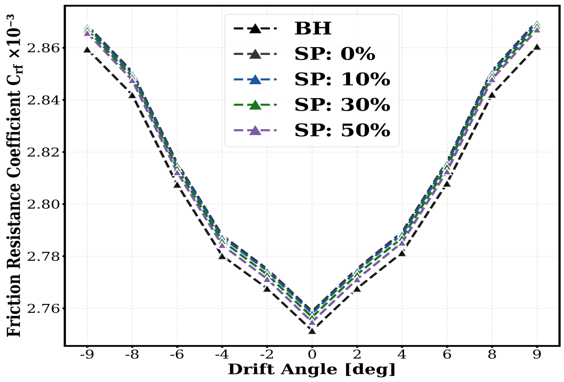

Figure 8: Bare hull (BH) and self-propelled hull (SP) frictional resistance coefficient for different sail thrust with drift angle variation

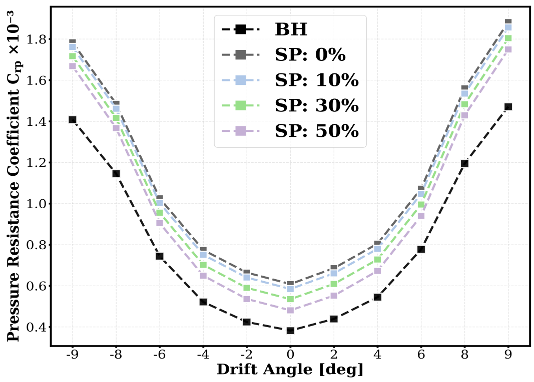

Figure 9: Bare hull (BH) and self-propelled hull (SP) pressure resistance coefficient for different sail thrust with drift angle variation

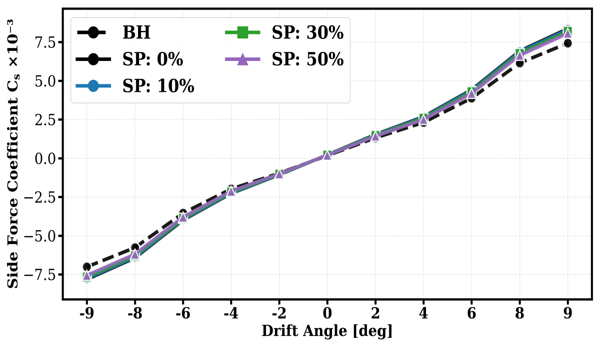

Figure 10: Bare hull (BH) and self-propelled hull (SP) side force coefficient for different sail thrust against drift angle variation

3.3 Thrust deduction

As explained in Section 2, the use of wind propulsion requires a set of analysis procedures to assess the ship's performance. The thrust deduction is obtained based on a standard procedure which is developed for conventional vessels with no wind assistance. The use of this procedure can lead to different interpretation when applied to a ship that benefits from wind propulsion as well. This subsection investigates the outcomes of using different definitions for thrust deduction for a wind-assisted ship.

Figure 12 shows the propeller thrust under self-propulsion. As expected, the thrust increases significantly with increasing drift angle, since the hull resistance increases.

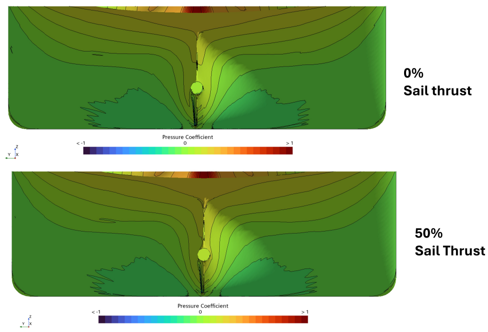

Figure 11: Pressure distribution over the aft hull at drift angle $0°$ for different sail thrust

Figure 13 presents the thrust deduction factor obtained based on Equation 2, where sail thrust is not included in the equation. For sail thrust levels of 0% and 10%, the thrust deduction has a slight change at high drift angles. As the sail thrust increases to 30% and 50%, the thrust deduction decreases significantly and even becomes negative. According to the conventional definition in ship hydrodynamics, the thrust deduction fraction represents the increase in required propeller thrust due to the suction effect of the propeller on the aft hull, relative to the bare-hull resistance. Under this definition, a negative thrust deduction value would imply that the required propeller thrust is lower than the bare-hull resistance, which is physically inconsistent.

Such a nonphysical result arises from neglecting the contribution of sail thrust in the evaluation of the thrust-deduction fraction. Therefore, this formulation is not appropriate for determining the thrust deduction fraction of wind-assisted ships. In the present study, it is used solely to demonstrate the resulting implications.

Using the formulation proposed by Sauder and Alterskjær (2022), the modified thrust deduction t^* provides a more appropriate representation. As shown in Figure 14, t^* increases with drift angle, reaching about 11% between $0°$ and $9°$ for sail thrust levels from 0% to 50%. A slight increase in t^* is also observed under sail thrust conditions, with a maximum variation of about 6%, while maintaining a consistent trend across all drift angles. Overall, higher sail thrust reduces the required propeller thrust, and this formulation yields a more consistent estimate of thrust deduction. However, linking t^* to the underlying physical mechanisms remains difficult compared to conventional vessels.

The resistance increment coefficient r was defined in Equation 4 and is shown in Figure 15. The resistance increment coefficient directly represents the ratio of bare-hull resistance to self-propelled hull resistance and therefore does not involve the ambiguities associated with the aforementioned thrust-deduction coefficient. An increase in r indicates that the bare-hull resistance R_{BH} has decreased relative to the self-propulsion resistance R_{SP}, implying the ship produces less resistance when the sail thrust increases. Conversely, a decrease in r indicates that R_{BH} has increased relative to R_{SP}, implying that the difference between R_{BH} and R_{SP} becomes smaller.

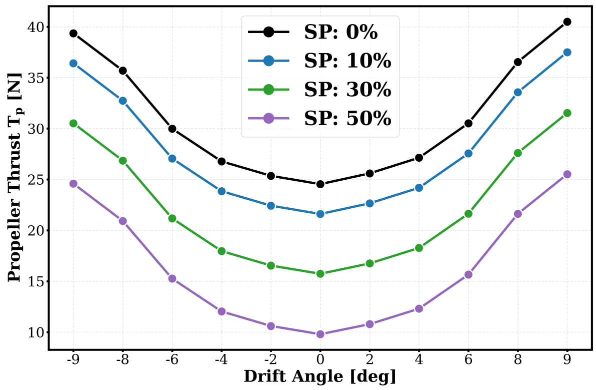

Figure 12: Propeller thrust T_p for different sail thrust

Overall, as a consequence of the stronger propeller suction effect acting on the aft hull, r becomes higher at lower sail thrust levels. For the case with 50% sail thrust, a difference of approximately 28% is observed between drift angles 0° and 9°. These results indicate that, higher sail thrust leads to a decrease in r. As the sail thrust increases, the difference in r between drift angles 0° and 9° increases. The variation of r with drift angle is limited to about 15%.

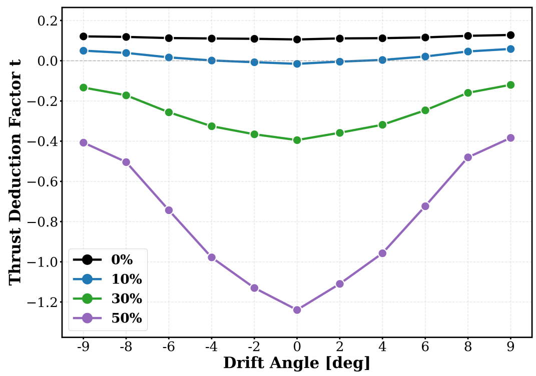

Figure 13: Classical thrust deduction t for different sail thrust

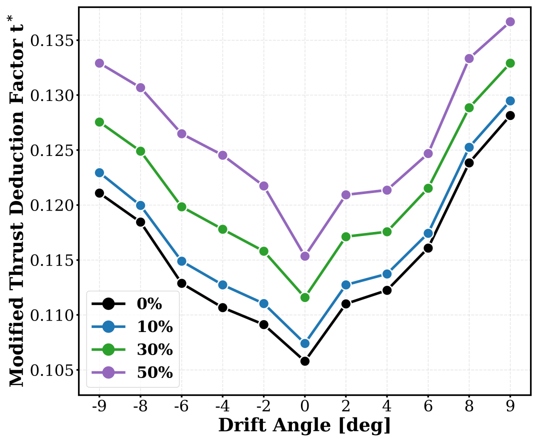

Figure 14: Thrust deduction t^* for different sail thrust

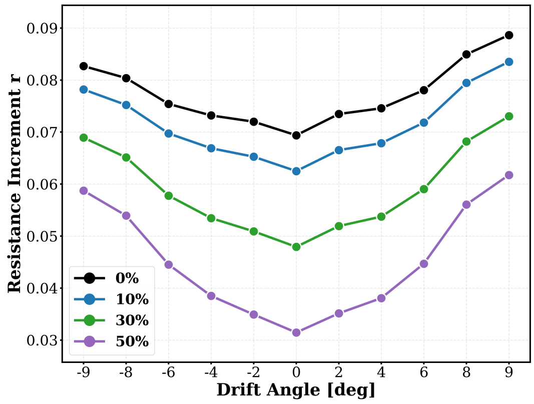

Figure 15: Resistance increment coefficient r for different sail thrust

Comparison of different thrust deduction definitions indicates that conventional thrust deduction is not fully applicable to wind-assisted ships, as the classical thrust deduction might become non-physical at high sail thrust. The thrust deduction formula t^* gives a more consistent result for all drift angles, however, it should not be mixed with the conventional thrust deduction while interpreting its value. The resistance increment coefficient directly compares the bare-hull and self-propelled hull resistances and is therefore more straightforward to interpret in terms of the underlying flow physics. The resistance increment coefficient r shows that there is a considerable decrease in self-propulsion resistance for all drift angles, especially at high sail thrust. The resistance increment coefficient r can only be obtained in numerical simulations, as it is difficult to measure or estimate self-propulsion resistance accurately in experimental tests.

4 COMPUTATION COST

Evaluation of the computational cost is an essential part of the study. In the present work, all simulations are performed without modelling the free surface, thereby significantly reducing computational cost. Each individual simulation requires approximately 190 core-hours. A total of 11 drift angles are considered for each sail thrust condition. With four sail thrust conditions, this results in 44 simulations, corresponding to a total of 8360 core-hours. In addition, bare-hull simulations are carried out for all 11 drift angles, requiring 2090 core-hours. An uncertainty analysis is also performed, consisting of 8 additional simulations, with a total cost of 1900 core-hours. The overall computational cost of the study, therefore, amounts to approximately 12350 core-hours, as shown in Table 5. Considering the number of simulated conditions and the scope of the analysis, the computational effort remains reasonable.

Table 5: Summary of computational cost for the CFD simulations

Simulations	Cases	Core-hours per case	Total
Sail thrust conditions	44	190	8360
Bare-hull simulations	11	190	2090
Uncertainty analysis	8	not fixed	1900
Total (core-hours)	**63**		**12 350**

5 CONCLUSION

In this study, the thrust deduction characteristics of wind-assisted ship propulsion were investigated. The simulations were carried out for bare-hull and self-propulsion conditions using a double-body approach, neglecting free-surface effects. The virtual propeller disk approach was used for the self-propulsion case. The study was conducted at a model scale with the Jores 1 tanker.

The bare-hull resistance increases substantially as the drift angle increases. The side force exhibits a similar trend and exceeds twice the resistance at higher drift angles. The comparison between the classical thrust deduction formula t and the modified formula t^* showed that the ship propulsion characteristics under wind-assisted conditions can be accurately represented only with the modified formula t^*. The classical formula for thrust deduction t was not appropriate to represent the wind-assisted ship propulsion characteristics since it generates non-physical results at high sail thrust levels. On the contrary, the modified formula t^* was seen to increase with an increase in sail thrust, up to 11%. The thrust deduction values obtained from the modified formula should not be interpreted in the same way as thrust deduction for conventional vessels.

As an alternative approach to study the resistance change between bare-hull and self-propelled hulls, resistance increment coefficient r is introduced in this work. Resistance increment coefficient shows a significant increase in self-propulsion resistance for all drift angles relative to bare-hull resistance. However, r can only be obtained from a numerical simulation and not as straightforward to obtain from towing tank tests.

In the future, free surface effects need to be included to take into account the effect of wave resistance and the effect of changes in the speed on the propulsion factors such as wake fraction, thrust deduction, and hull efficiency. Additionally, a more accurate propeller model, together with a rudder, will be used to better capture the interaction effects.

ACKNOWLEDGEMENTS

This work was supported by the Swedish Transport Agency through Lighthouse – Swedish maritime competence centre. The authors acknowledge the National Academic Infrastructure for Supercomputing in Sweden (NAISS) under the project (Naiss2025-5-609 and Naiss2025-5-67) and the Chalmers Centre for Computational Science and Engineering (C3SE) under the project (C3SE2026-1-1) for providing the computational resources used in this study.

REFERENCES

Fadaie, S., Thornley, P., & Souppez, J.-B. (2025). 'A systematic review of technologies, measures, and CO2 emission reduction potential for maritime transport decarbonisation'. Advances in Applied Energy **100255**.

Ammar, N.R. & Seddiek, I.S. (2022). 'Wind-assisted propulsion system onboard ships: Case study of Flettner rotors'. Ships and Offshore Structures **17**(7): pp. **1616–1627**.

Bakari, A.-M., Lopes, R., Eslamdoost, A. & Bensow, R. (2025). 'Toward obtaining the propulsive factors for a wind-assisted ship' The Proceedings of 27th Numerical Towing Tank Symposium, Zagreb, Croatia: pp. **14–19**.

Bordogna, G. (2020). Aerodynamics of Wind-Assisted Ships: Interaction Effects on the Aerodynamic Performance of Multiple Wind-Propulsion Systems. PhD Thesis, Delft University of Technology, Netherlands.

Clayton, B.R. (1987). 'Wind-assisted ship propulsion'. Physics in Technology **18**(2), p. 53.

IMO (2023). 2023 IMOStrategy on Reduction of GHG Emissions from Ships. Resolution MEPC.377(80), Marine Environment Protection Committee (MEPC).

JoRes Project. (2023). 'Ship scale validation cases for energy efficiency solutions'.
Joint Research Project. Available at: https://jores.net/

Sauder, T. and Alterskjær, S.A. (2022). Hydrodynamic testing of wind-assisted cargo ships using a cyber–physical method'. Ocean Engineering **243**: p. 110206.

ITTC (2011). Recommended Procedures and Guidelines: 7.5–03–02–03 Practical Guidelines for Ship CFD Applications. 26th ITTC Specialist Committee on CFD in Marine Hydrodynamics.

ITTC (2022). Recommended Procedures and Guidelines 0.0: Register (Revision 10).
29th International Towing Tank Conference.

Ouchi, K., Uzawa, K., Kanai, A. & Katori, M. (2013).'Wind Challenger: The next generation hybrid sailing vessel'.
Proceedings of 3rd International Symposium on Marine Propulsors, Launceston, Tasmania, Australia: pp. **562–567**.

Eça, L. & Hoekstra, M. (2014). 'A procedure for the estimation of the numerical uncertainty of CFD calculations based on grid refinement studies'. Journal of Computational Physics **262**, pp. 104–130.

HSVA. (2023). 'Model Tests for JoRes Tanker 1'.
HSVA Report No. RP-2023-033, JoRes Joint Research Project.

Saydam, A.Z., Kellett, P., Banks, C., Boulougouris, E. & Incecik, A. (2022). 'Investigation of the influence of wind-assisted propulsion devices on hull design'. Contemporary Studies in Shipping, Ports and Logistics: pp. **211–216**.

Yao, J.X., Jin, W., Song, Y. (2016). RANS simulation of the flow around a tanker in force motion. *Ocean Engineering*, **227 236–245**.